CASL-U-2014-0210-000

Power uprates
and plant life extension

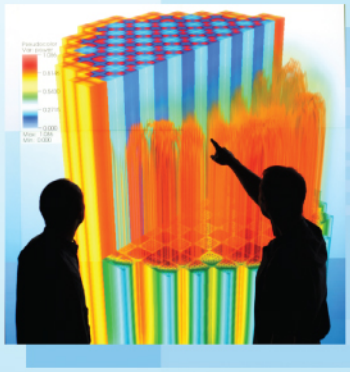

Engineering design
and analysis

Science-enabling
high performance
computing

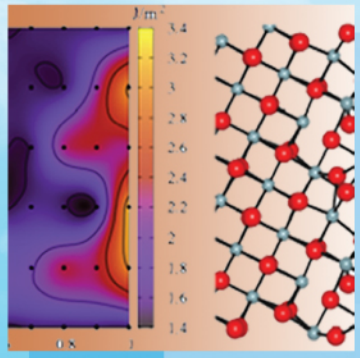

Fundamental science

Plant operational data

Consortium for Advanced Simulation of LWRs

L3:THM.CFD.P9.05 Milestone Report Single/Multiphase CFD Assessment, Verification, and Validation

Yidong Xia and Hong Luo
North Carolina State University

September 30, 2014

U.S. DEPARTMENT OF ENERGY | Nuclear Energy

Single/Multiphase CFD assessment, verification, and validation

L3:THM.CFD.P9.05 milestone report

Yidong Xia and Hong Luo

Department of Mechanical and Aerospace Engineering
North Carolina State University, Raleigh, NC, 27695, USA

On the performance of a set of RANS and LES models for simulating incompressible turbulent flows

Yidong Xia[a,*], Hong Luo[a], Mark Christon[b], Jozsef Bakosi[b]

[a] *Department of Mechanical and Aerospace Engineering*
North Carolina State University
Engineering Bldg 3, Campus Box 7910
911 Oval Drive
Raleigh, NC 27695-7910
[b] *Computational Physics Group (CCS-2)*
Computer, Computational and Statistical Sciences Division
Los Alamos National Laboratory
P.O. Box 1663
Los Alamos, NM 87545

Abstract

Hydra-TH is a hybrid finite-volume/finite-element incompressible/low-Mach flow solver based on the Hydra toolkit that is being developed and used for thermal-hydraulics applications. In this work, a suite of verification and validation (V&V) problems for Hydra-TH is defined to meet the design requirements, and solved to the interests of the Consortium for Advanced Simulation of Light Water Reactors (CASL). The intent for this suite of problems is to provide baseline comparison data that demonstrates the performance of the Hydra-TH solution methods on a series of test cases that vary in complexity from laminar to turbulent flows, in which a set of RANS and LES turbulence models are used in computation of four classical test cases. Numerical results obtained by Hydra-TH agree well with either the available analytical solution or experimental data, indicating the verified and validated implementation of these turbulence models in Hydra-TH. Where possible, some form of solution verification has been attempted to identify sensitivities in the solution methods, and suggest best practices when using Hydra-TH.

Keywords:

*corresponding author
Email address: yxia2@ncsu.edu (Yidong Xia)

1. Introduction

Hydra-TH [1, 2, 3, 4, 5, 6, 7, 8, 9] refers to the hybrid finite-element/finite-volume incompressible/low-Mach flow solver in the Hydra toolkit that is being used for thermal-hydraulics applications for the Consortium for Advanced Simulation of Light Water Reactors (CASL) [10]. Hydra-TH is built as one of a number of virtual physics using the Hydra multi-physics toolkit. The Hydra toolkit is written in C++ and provides a rich suite of components that permits rapid application development, supports multiple discretization techniques, provides I/O interfaces to permit reading/writing multiple file formats for meshes, plot data, time-history, surface-based and restart output. Data registration is used to provide the ability to register variables at appropriate locations (e.g., node, element, dual-edge, etc), and provides integrated and automatic output and restart capabilities along with memory management. The toolkit also provides run-time parallel domain decomposition with data-migration for both static and dynamic load-balancing. Linear algebra is handled through an abstract virtual interface that makes it possible to use popular libraries such as PETSc [11] and Trilinos [12]. The use of output delegates provides the ability to develop lightweight physics-specific output kernels with minimal memory overhead that can be tailored to a specific physics, e.g., computation of vorticity, helicity, enstrophy for large-eddy simulations.

Verification testing is part of the Hydra software control process and ensures that Hydra-TH is solving problems of interests to the CASL project and meeting design requirement. It is one component of a larger testing infrastructure. This paper is aimed to identify verification problems and the Hydra-TH solutions to those problems. We anticipate that there will be more test problems added to the suite of verification and validation for flow simulation, as the Hydra-TH code will change over time. The tests are organized by methods and physics to enable a quick survey of code capabilities.

The rest of this paper is organized as follows: Section 2 first introduces the baseline numerical method employed by Hydra-Th, and then the RANS and LES turbulence models implemented in the current suite. Section 3 presents four classical test cases computed by Hydra-TH: 1) the steady-state Poisueille flow; 2) a laminar flow past a flat plate at Reynolds number of Re

= 100,000, which can be compared with the classical Blasius solution; 3) a wall-bounded turbulent channel flow at $Re_\tau = 590$, where two RANS turbulence models are verified and validated according to the referenced Direct Numerical Simulation (DNS) data; 4) large-eddy simulation of a lid-driven cavity flow, in which three LES models in Hydra-TH are tested and verified with respect to the referenced experimental data. Section 4 gives a conclusion of the work in this paper, and outlook for future work.

2. Numerical method

Hydra-TH uses a hybrid finite-element/finite-volume discretization for the incompressible/low-Mach Navier-Stokes equations. All transport variables are cell-centered and treated with a conservative discretization that includes a high-resolution monotonicity-preserving advection algorithm. The spatial discretization is formally derived using a discontinuous Galerkin framework that, in the limit, reduces to a locally conservative finite volume method. The high-resolution advection algorithm is designed to permit both implicit and explicit advection with the explicit advection targeted primarily at volume tracking with interface reconstruction. The time-integration methods include backward-Euler and neutrally-dissipative trapezoidal method. The implicit advective treatment delivers unconditional stability for the scalar transport equations, and conditional stability for the momentum transport equations. A sharp stability estimate for the momentum equations is not tractable, but operational experience shows that the algorithm is stable for $20 \leq CFL \leq 40$. For steady-state problems, backward-Euler provides additional damping that, in conjunction with $20 \leq CFL \leq 40$, provides a computationally efficient solution method. For Unsteady Reynolds-Averaged Navier-Stokes (URANS) and Large-Eddy Simulation (LES) computations, the trapezoid rule is neutrally dissipative, and delivers optimal performance for the more moderate CFL requirements for transient flow.

Hydra-TH is designed to incorporate both well-established and state-of-the-art turbulence models, ranging from traditional RANS through LES to hybrid RANS-LES models. The following models implemented in Hydra-TH have been used in this work:

- RANS models
  - Spalart Allmaras model [13]

  - Re-normalized group (RNG) k-ε model [14]

- LES models
  - MILES or ILES [15]: This family of models is obtained using a monotonicity preserving advection treatment (MILES) and is also referred to as implicit LES (ILES).
  - Smagorinsky model [16]
  - Wall-adapted large eddy (WALE) model [17]

The use of LES implies a required suit of post-processing tools for extracting useful averages and statistics. Hydra-TH provides an interface for performing windowed time-averaging suitable for post-simulation generation of ensemble averages. The calculation of derived statistics is outlined in §6.6 of the Hydra-TH theory manual [1].

3. Computational results

3.1. Poisueille Flow

The objective of this numerical experiment is to verify if Hydra-TH can achieve a formal order of the convergence rate for incompressible laminar flows. The test problem chosen in this case is the steady Poisueille flow, which represents an exact solution to the full system of two-dimensional incompressible Navier-Stokes equations for a laminar flow in a channel. The velocity distribution at any given streamwise locations is a parabolic profile given by

$$v_{exact} = 12\mu - \frac{dP}{dx}(H - y)$$

where $1/\mu = Re$, and H is the height of the channel.

In this experiment, the Reynolds number based on the height of the channel is 100, the pressure gradient based on the length of the channel dP/dx is -0.12, and the height of the channel H is 1. The computational domain is bounded from 0 to 20 in x-direction, from 0 to 1 in y-direction, and from 0 to 1 in z-direction. A series of four successively refined hexahedral grids, consisting of $100 \times 5 \times 1$, $200 \times 10 \times 1$, $400 \times 20 \times 1$, and $800 \times 40 \times 1$ elements, respectively, and shown in Figures 1(a) - 1(d) , is used to conduct the convergence study.

All contour and line plots are based on the cell-centered solutions. The x-velocity and pressure contours for the four grids are shown in Figures 2(a) - 2(d) and 3(a) - 3(d), respectively. The computed x-velocity distributions on the four grids are compared with the exact solution at outflow boundary cells, as shown in Figures 4(a) - 4(d).

The convergence order of accuracy can be assessed by computing the slope of logarithmic L^2 norm of the error function in terms of the logarithmic cell size, where the L^2 error can be computed as

$$errl2 = \| V_x - v_{exact} \|_2 = \sqrt{\sum_{i=1}^{ncell} \int_{\Omega} (V_x - v_{exact})^2 \, d\Omega} = \sqrt{\sum_{i=1}^{ncell} (V_x - v_{exact})^2 \Omega_i}$$

where n_{cell} is the total cell number of the grid and Ω_i is the volume of each cell. Then, the piecewise order or the slope can be computed using two successively refined grids of characteristic cell size h and $h/2$ as follows

$$slope = \frac{\log_{10} errl2_{\frac{h}{2}} - \log_{10} errl2_h}{\log_{10} \frac{h}{2} - \log_{10} h}$$

Table 1 shows the L^2 errors and convergence orders of accuracy obtained from these four grids, indicating that Hydra-TH is able to achieve the designed second-order of accuracy of convergence for solving the incompressible Navier-Stokes equations.

Table 1: Convergence order analysis of Poisueille flow in a channel for four successively refined grids: $100 \times 5 \times 1$, $200 \times 10 \times 1$, $400 \times 20 \times 1$, and $800 \times 40 \times 1$

Cell Size	$\log_{10}(L^2 - error)$	Order
0.2	-0.58886	—
0.1	-1.23673	2.152
0.05	-1.81820	1.932
0.025	-2.41830	1.994

3.2. Flow Past A Flat Plate

The laminar boundary layer over an adiabatic flat plate is considered in this test case. This problem is chosen to assess the accuracy of the Hydra-TH solution methods for the discretization of the viscous and heat fluxes in

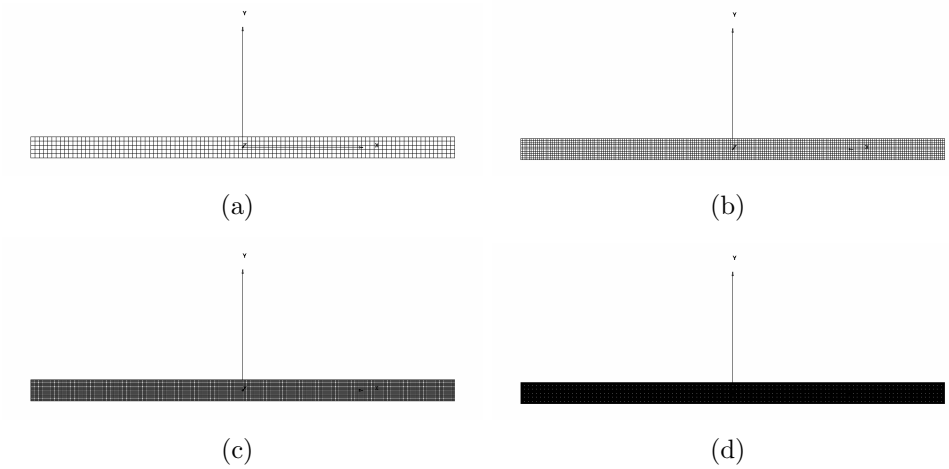

Figure 1: Plots of the four successively refined hexahedral grids for steady Poiseuille flow in a channel: (a) $100 \times 5 \times 1$, (b) $200 \times 10 \times 1$, (c) $400 \times 20 \times 1$ and (d) $800 \times 40 \times 1$

.

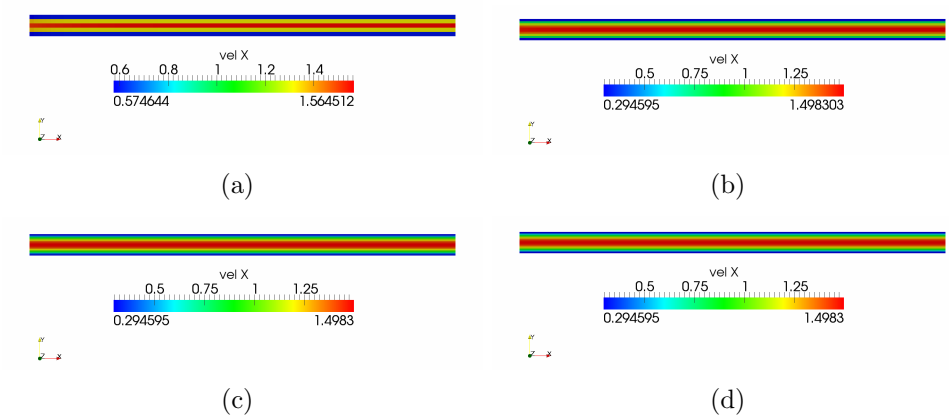

Figure 2: Plots of x-velocity contours of steady Poiseuille flow in a channel for four successively refined grids: (a) $100 \times 5 \times 1$, (b) $200 \times 10 \times 1$, (c) $400 \times 20 \times 1$ and (d) $800 \times 40 \times 1$

.

the incompressible Navier-Stokes equations, as the classical Blasius solution can be used to measure the accuracy of the numerical solution. Comparative study is also performed among a series of three grids to demonstrate that the grid stretching ratio (SR) normal to the no-slip surface can have a significant effect on the quality of solution.

In this experiment, the Reynolds number based on the length of the flat

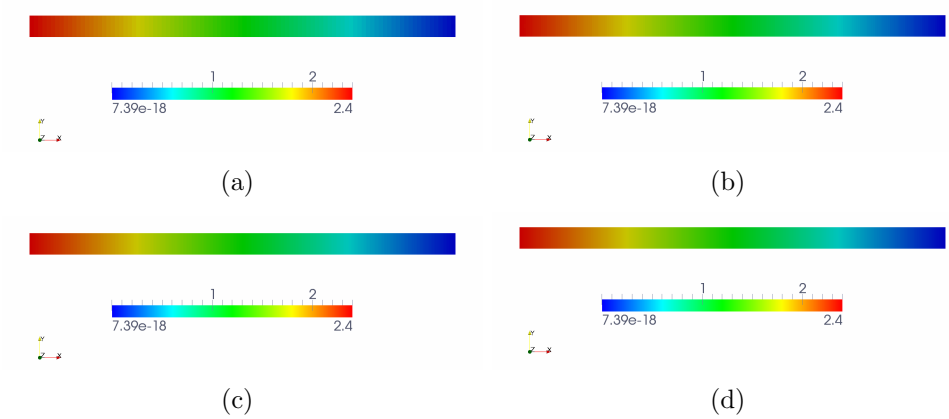

Figure 3: Plots of pressure contours of steady Poisueille flow in a channel for four successively refined grids: (a) $100 \times 5 \times 1$, (b) $200 \times 10 \times 1$, (c) $400 \times 20 \times 1$ and (d) $800 \times 40 \times 1$

.

plate is $Re = 100,000$. The computational domain is bounded from -0.5 to 1.0 along the x-direction, from 0 to 1.0 along the y-direction, and from 0 to 0.1 along the z-direction, and the no-slip surface starts at point $(0, 0, z)$ and extends to $(1, 0, z)$. The three hexahedral grids used in this computation have the same number of cells $(25 + 50) \times 30 \times 1$, with $25 \times 30 \times 1$ cells ahead of the flat plate and $50 \times 30 \times 1$ cells for the flat plate, the same distribution of the grid points in the x-direction, but a different distribution of grid points in the y-direction. In order to cluster points near the flat plate, the point distribution in the y-direction follows a geometric stretching. The stretching ratio (SR) is the ratio of the heights of the two successive elements. An SR value of 1.15, 1.20 and 1.30 is used for the three grids in the computation, respectively. The grids are plotted in Figures 5(a) through 5(c). A complete quantitative description is shown in Table 2. For example, for the grid of SR = 1.15, the height of the first element is 2.3002×10^{-3}, and it is also characterized with the normalized height of $y^+ = 12.35$. As a result, the grid of SR = 1.30 provides the best grid resolution in the boundary layer region.

The inflow boundary condition when $x = 0$ is prescribed with $\mathbf{V} = (1, 0, 0)$. No-slip and no-penetration conditions $\mathbf{V} = (0, 0, 0)$ are prescribed when $y = 0$ for $x \in [0, 1]$. A slip condition is prescribed along the bottom side of the domain for $x \in [-0.5, 0]$ with $V_y = 0$. Symmetry conditions are prescribed in the 1-cell thick region with $v_z = 0$. The pressure at outflow boundary is prescribed to be $P = 0$ on the top side ($y = 1$) and right side

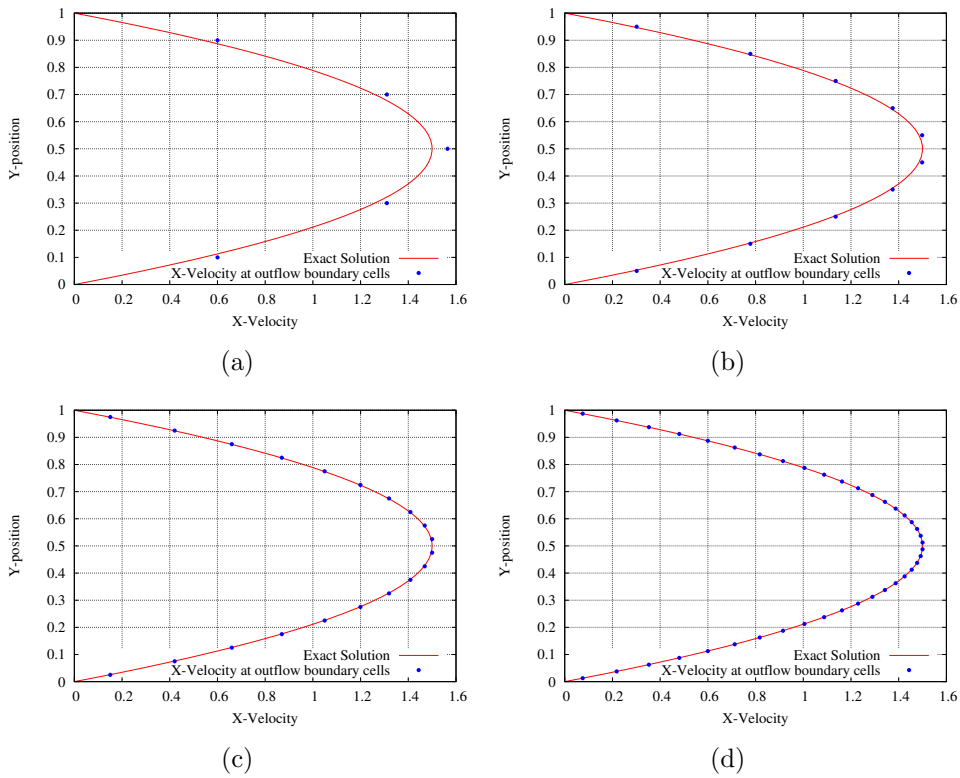

Figure 4: Plots of x-velocity profiles at outflow boundary cells of steady Poisueille flow in a channel for four successively refined grids: (a) $100 \times 5 \times 1$, (b) $200 \times 10 \times 1$, (c) $400 \times 20 \times 1$ and (d) $800 \times 40 \times 1$

.

$(x = 1)$.

All plots are computed using cell-centered values, and the velocity results plotted with the Blasius boundary solution. Figure 6 shows the time history of kinetic energy obtained from the solutions on three grids. As one can observe, the kinetic energy computed from the grid of SR = 1.15 is clearly lower than from the other two grids, indicating a under resolved boundary layer. Figure 7 shows the logarithmic plots of the computed skin friction coefficient c_f distributions along the flat plate $x \in [0, 1]$. The skin friction coefficient c_f is defined by

$$c_f = \frac{\tau_w}{\frac{1}{2}\rho U_\infty^2}$$

where τ_w is the local wall shear stress, ρ is the fluid density $(\rho = 1)$ and U_∞

Table 2: Boundary layer of the grid for steady flow past a flat plate at $Re = 100,000$

Stretching Ratio (SR)	y of the first layer	y^+ of the first layer
1.15	2.3002×10^{-3}	12.35
1.20	8.4611×10^{-4}	4.542
1.30	1.1455×10^{-4}	0.615

is the free-stream velocity ($U_\infty = 1$). The wall shear stress τ_w is given by

$$\tau_w = \mu \left(\frac{\partial u}{\partial y} \right)_{y=0}$$

where μ is the dynamic viscosity ($\mu = \frac{1}{Re}$), u_w is the $x-$direction flow velocity at the center of the cell adjacent to plat plate, and Δy_w is the y coordinate of the corresponding cell center (Δy_w equals half of the first layer height). As expected, the grid of SR = 1.30 provided the best prediction of c_f. The grid of SR = 1.20 overpredicted the c_f distribution near the plate leading edge due to the insufficient grid resolution. The grid of SR = 1.15 presented the worst c_f distribution because the grid resolution near the leading edge region is rather poor.

Figures 8 through 9 show the plots of computed V_x and V_y profiles along the cells cut through by plane of $x = 0.10$, $x = 0.50$ in the boundary layer region. Similar to the c_f results, the grid of SR=1.15 is under resolved and hence V_y is significantly over-predicted. In comparison, the y-velocity is much better for the grid of SR = 1.20 and 1.30, which can match the analytical solution well.

3.3. Turbulent Channel Flow at $Re_\tau = 590$

The test case chosen in this numerical experiment is the well-documented turbulent channel flow at a friction Reynolds number of $Re_\tau = 590$ [18]. The Spalart-Allmaras one-equation model and the RNG k-ε two-equation model with a wall function are used for RANS simulation in this test case, respectively.

This 2-D turbulent flow problem considered here consists of a 2-D duct with a 20 : 1 aspect ratio, $Re = 10^4$, and $\partial p/\partial x = -2.785 \times 10^{-2}$. This choice of laminar Reynolds number and pressure gradient results in an approximate posteriori friction Reynolds number at $Re_\tau = 590$. In this study, computation

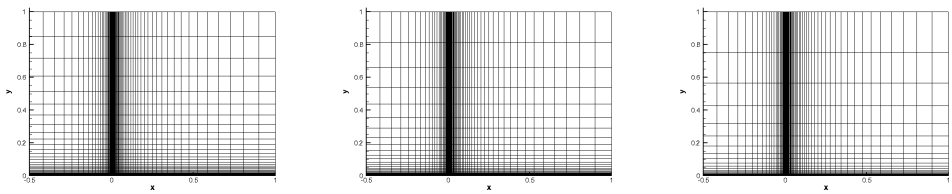

(a) (b) (c)

Figure 5: Plot of the $(25 + 50) \times 30 \times 1$ hexahedral grids for steady flow past a flat plate at $Re = 100,000$: (a) SR $= 1.15$ in y-direction; (b) SR $= 1.20$ in y-direction; (c) SR $=$ 1.30 in y-direction

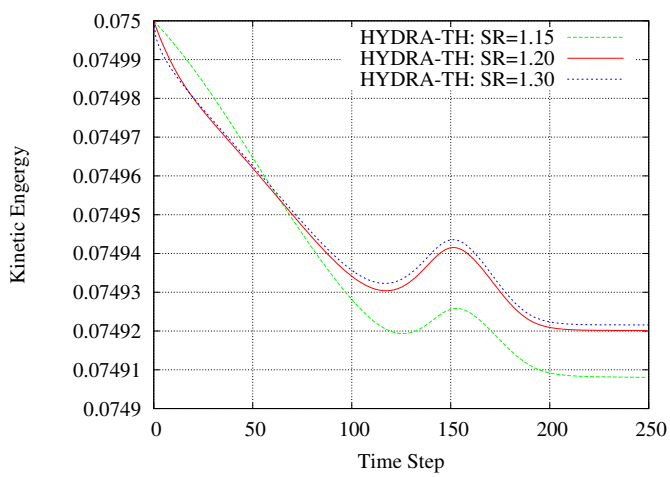

Figure 6: Time history plots for kinetic energy obtained on the $(25+50)\times30\times1$ hexahedral grids

is conducted for each of the turbulence models on a series of three successively refined hexahedral grids, as described in Table 3 and Table 4, respectively. The channel dimensions are 20 units in the x direction, 1 unit in the y direction, and 0.05 unit in the z direction, as shown in Figure 10. The grid is uniform in the streamwise x directions.

In order to represent the constant pressure gradient, an inflow pressure boundary condition of $p = 0.557$ is prescribed with $V_y = 0$ and $V_z = 0$. No-slip/no-penetration conditions $\mathbf{V} = (0, 0, 0)$ are prescribed along the top and bottom duct walls. The so-called "natural" velocity boundary conditions are

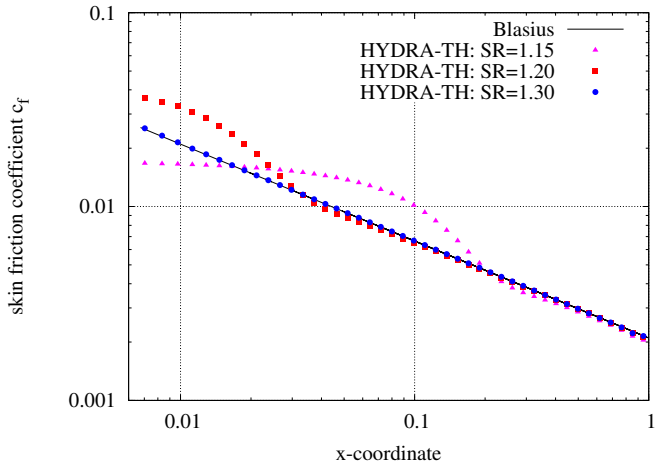

Figure 7: Logarithmic plot of the computed skin friction coefficient distribution obtained on the $(25+50)\times 30\times 1$ hexahedral grids compared with the analytical solution along the flat plate $x=[0,1]$

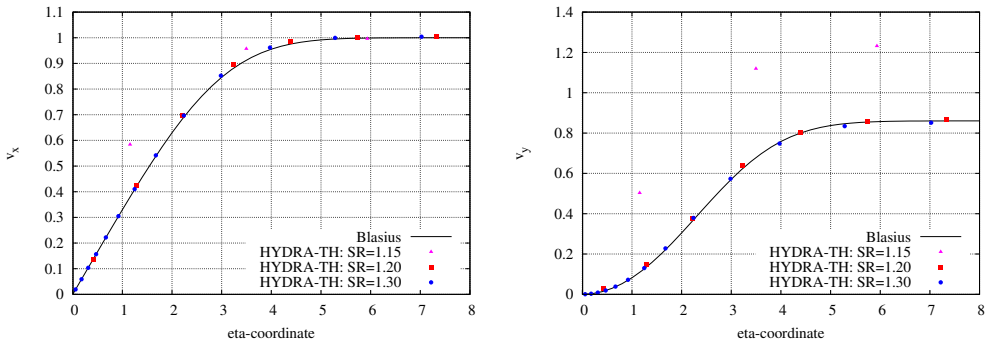

(a) (b)

Figure 8: Plot of the (a) V_x and (b) V_y profiles obtained on the $(25+50)\times 30\times 1$ hexahedral grids compared with the analytical solutions along the cells cut through by plane of $x=0.10$ in the boundary layer region

applied at the outflow boundary, with the prescribed pressure $p=0$. The slip/no-penetration conditions ($V_x=0$ and $V_y=0$) are prescribed on the front and back duct walls. The initial condition is that the velocity field is at rest with no random perturbations.

The end-time for all tests is $t=500.0$ when the problem is fully converged.

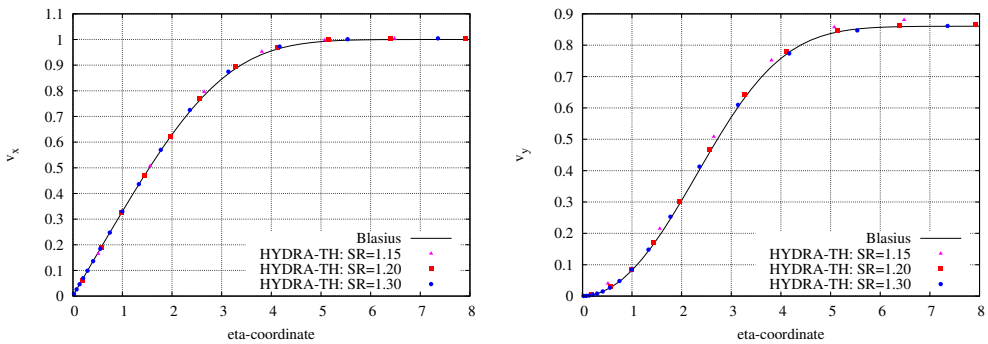

(a) (b)

Figure 9: Plot of the (a) V_x and (b) V_y profiles obtained on the $(25 + 50) \times 30 \times 1$ hexahedral grids compared with the analytical solutions along the cells cut through by plane of $x = 0.50$ in the boundary layer region

Figure 11 and 12 show the time history of global kinetic energy. The cell-centered solution data of mean streamwise velocity V_x (Figure 13 and 14) turbulent eddy viscosity ν_t (Figure 17 and 18), turbulent kinetic energy k (Figure 19) and turbulent kinetic energy dissipation rate ε (Figure 3.3). The last two are only available for RNG k-ε model. is extracted and plotted versus normal distance from the bottom wall to half width of the channel at $x = 5$, which is 3/4 of the channel length. The normalized velocity profiles in comparison with the DNS result by Moser et al. [18] are shown in Figure 15 and 16.

The end-time for all tests is $t = 500.0$ when the problem is fully converged. Figure 11 and 12 show the time history of global kinetic energy. The cell-centered solution data of mean streamwise velocity V_x (Figure 13 and 14), , turbulent eddy viscosity ν_t (Figure 17 and 18), turbulent kinetic energy k (Figure 19) and turbulent kinetic energy dissipation rate ε (Figure 3.3). The last two are only available for RNG k-ε model. is extracted and plotted versus normal distance from the bottom wall to half width of the channel at $x = 5$, which is 3/4 of the channel length. The normalized velocity profiles in comparison with the direct numerical simulation (DNS) result by Moser et al. [18] are shown in Figure 15 and 16. The non-dimensional velocity V_x^+ is defined as $V_x^+ = V_x/u_\tau$, where u_τ is the friction velocity. u_τ is computed from the equation for friction Reynolds number $Re_\tau = u_\tau\delta/\nu$, where $\delta = 1/2$ is the half width of channel and $\nu = 10^{-4}$ is prescribed. The non-dimensional

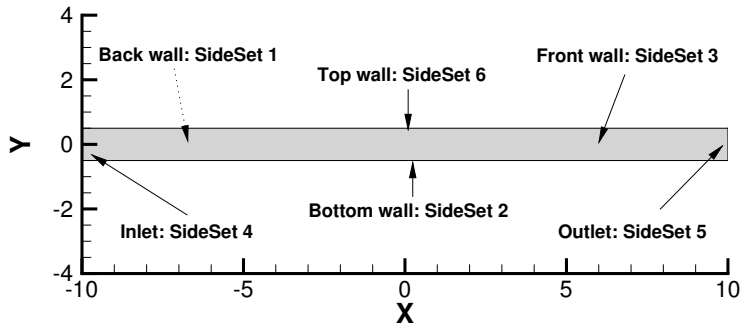

Figure 10: The bounded domain for simulation of a turbulent channel flow.

wall distance y^+ is defined as $y^+ = u_* y/\nu$, where u_* is the friction velocity at the nearest wall (equal to the u_τ in this context), and y is the distance to the nearest wall. It is observed that the profiles obtained from the 50×201 and 50×401 grids almost coincide in Figure 13, 15 and 17, respectively. Moreover, both the unscaled and scaled velocity profiles by Spalart-Allmaras model can match the DNS results quite well. In Figure 16, it is observed that the scaled velocity profiles by RNG k-ε model show the convergence of solution and can match the DNS profile in the log layer region, but they do not tend to approach the DNS profile once in the sublayer, due to the limitations of using wall functions which is stated in §12.4 of Hydra-TH theory manual [1].

Table 3: Grids used for turbulent channel flow, $Re_\tau = 590$, Spalart-Allmaras model.

Grid size	y of the first-layer	y^+ of the first layer
$50 \times 101 \times 1$	1.162×10^{-3}	1.371
$50 \times 201 \times 1$	9.343×10^{-5}	0.110
$50 \times 401 \times 1$	2.823×10^{-4}	0.333

3.4. Large-Eddy Simulation of a Lid-Driven Cavity Flow

This numerical experiment is the large-eddy simulation of a lid-driven cavity flow at a Reynolds number of $Re = 10,000$. A grid refinement study is performed using Hydra-TH with the three turbulence models, implicit

Table 4: Grids used for turbulent channel flow, $Re_\tau = 590$, RNG k-ε model.

Grid size	y of the first layer	y^+ of the first layer
$50 \times 41 \times 1$	1.220×10^{-2}	14.390
$50 \times 81 \times 1$	6.173×10^{-3}	7.284
$50 \times 161 \times 1$	3.106×10^{-3}	3.665

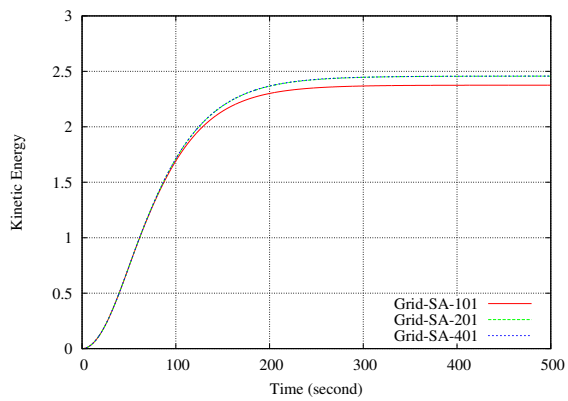

Figure 11: Time history of global kinetic energy for simulation of a turbulent channel flow, $Re_\tau = 590$, Spalart-Allmaras model.

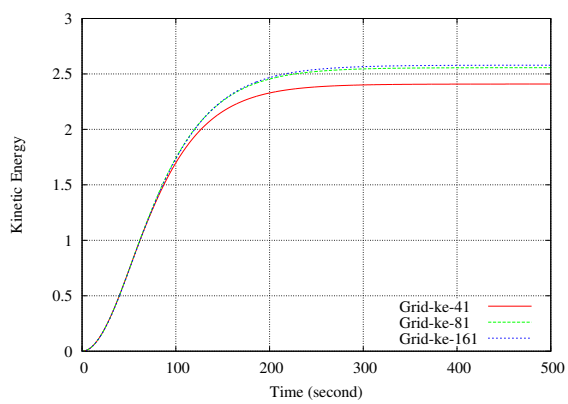

Figure 12: Time history of global kinetic energy for simulation of a turbulent channel flow, $Re_\tau = 590$, RNG k-ε model.

large-eddy simulation (ILES), wall-adapted large eddy (WALE) subgrid-scale model and the Smagorinsky subgrid-scale model, respectively.

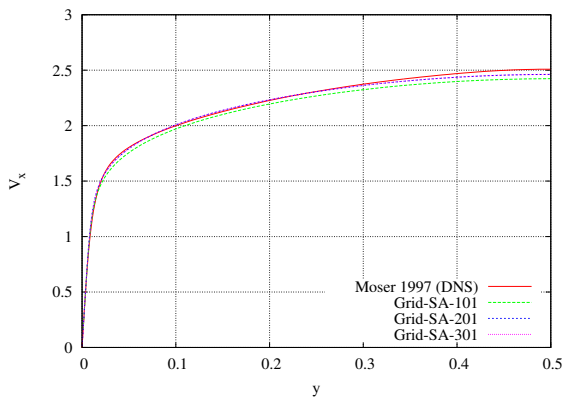

Figure 13: V_x versus normal distance from bottom wall for simulation of a turbulent channel flow, $Re_\tau = 590$, Spalart-Allmaras model.

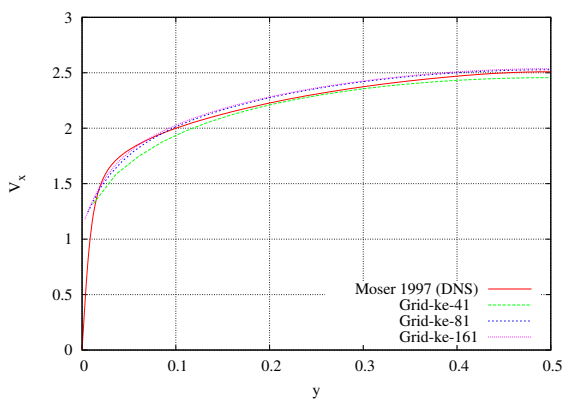

Figure 14: V_x versus normal distance from bottom wall for simulation of a turbulent channel flow, $Re_\tau = 590$, RNG k-ε model.

In this study, computation is conducted for each of the turbulence models on a series of three successively refined hexahedral grids, as shown in Figures. 21 and 22, for which the numbers of total cells are $32 \times 32 \times 16$ (coarse), $64 \times 64 \times 32$ (medium), and $128 \times 128 \times 64$ (fine) respectively. The cavity dimensions are 1 unit in the x and y directions, and 0.5 unit in the z direction. The grid is non-uniform in the streamwise x and vertical y directions, but is spanwise z direction uniform. Grid points are clustered near the walls in the x and y directions. The grid spacing is geometrically stretched away from the wall, where the minimum value is 5.0×10^{-3} for the coarse and medium

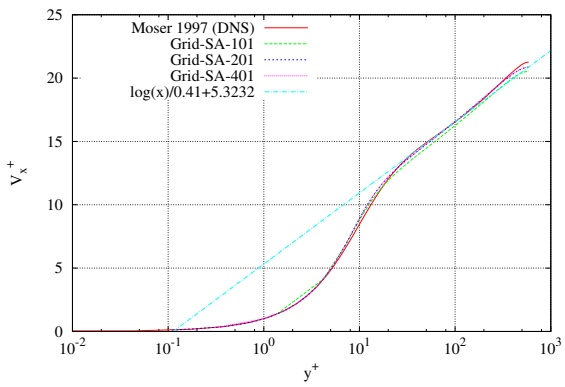

Figure 15: V_x^+ versus y^+ from bottom wall for simulation of a turbulent channel flow, $Re_\tau = 590$, Spalart-Allmaras model.

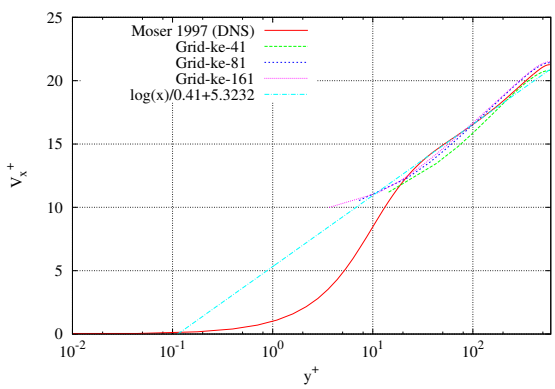

Figure 16: V_x^+ versus y^+ from bottom wall for simulation of a turbulent channel flow, $Re_\tau = 590$, RNG k-ε model.

grids, and 5.0×10^{-4} for the fine grid. On the bottom and side walls, no-slip/no-penetration boundary conditions are prescribed. Along the top "lid", a no-penetration boundary condition along with a unit lid velocity $u_b = 1$ are prescribed. The initial condition is that the velocity field is at rest with no random perturbations.

All the tests in this experiment are run for approximately 500 time units with 20 time planes containing average statistics being written between the 100th and 500th time unit. Figures. 23, 24 and 25 show the time histories of kinetic energy with each turbulence model, respectively. The cell-centered

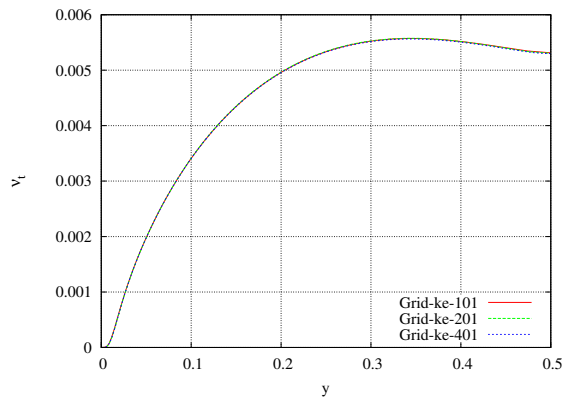

Figure 17: Turbulent eddy viscosity versus normal distance from bottom wall for simulation of a turbulent channel flow, $Re_\tau = 590$, Spalart-Allmaras model.

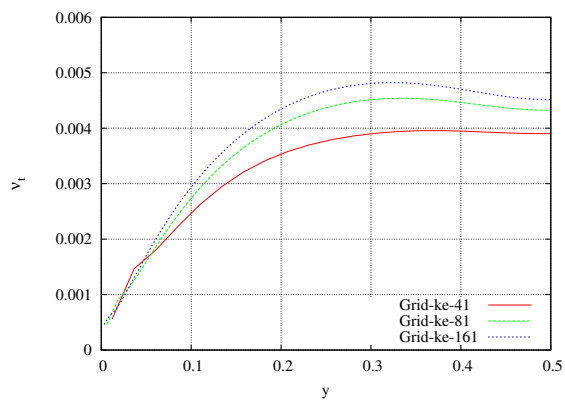

Figure 18: Turbulent eddy viscosity versus normal distance from bottom wall for simulation of a turbulent channel flow, $Re_\tau = 590$, RNG k-ε model.

solution of the mean velocity vector and Reynolds stress tensor is extracted and plotted along the centerlines on the spanwise mid-plane for direct comparison with the experimental data published by Prasad and Koseff [19], as shown in Figures. 26 - 28 for the ILES model, Figures. 29 - 31 for the WALE model, and Figures. 32 - 34 for the Smagorinsky model. The $x-$ mean velocity $\langle u \rangle$ distribution is plotted along the vertical centerline, and the $y-$ mean velocity $\langle v \rangle$ distribution is plotted along the horizontal centerline as shown in Figures. 26, 29 and 32. Improvement of the mean velocities is clearly observed from the coarse grid to the medium grid for all of the three models.

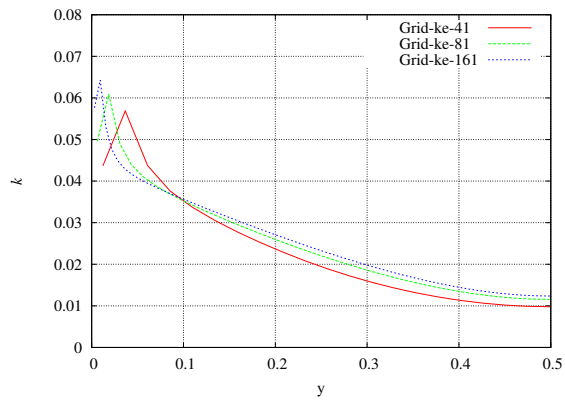

Figure 19: Turbulent kinetic energy versus normal distance from bottom wall for simulation of a turbulent channel flow, $Re_\tau = 590$, RNG k-ε model.

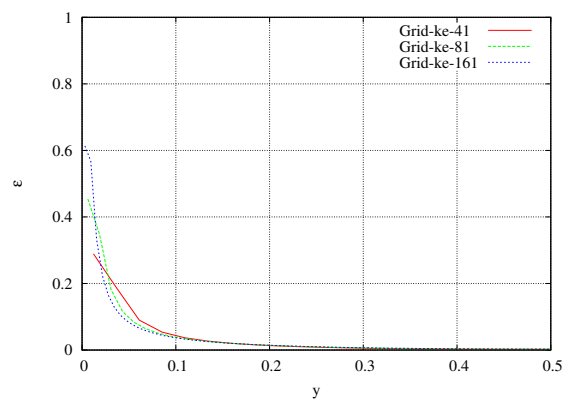

Figure 20: Turbulent kinetic energy dissipation rate versus normal distance from bottom wall for simulation of a turbulent channel flow, $Re_\tau = 590$, RNG k-ε model.

The mean velocities vary only a little from the medium grid to the fine grid for these models, but already agree quite well with the experimental data. The scaled $\langle u'u' \rangle$ distribution is plotted along the vertical centerline, and the scaled $\langle v'v' \rangle$ distribution is plotted along the horizontal centerline as shown in Figures. 27, 30 and 33. The scaled $\langle u'v' \rangle$ distribution is plotted along the vertical and horizontal centerlines as shown in Figures. 28, 31 and 34. Observation indicates that the $\langle u'u' \rangle$ and $\langle u'v' \rangle$ profiles are significantly improved from the coarse grid to the medium grid. Also, a distinguished improvement of the $\langle u'u' \rangle$ and $\langle u'v' \rangle$ profiles can be seen from the medium grid to the fine

grid, if compared with the experimental data. Further, comparison between the results obtained from these three models indicates that the performance of the ILES and WALE models is close to each other, but they have delivered a better numerical prediction than the Smagorinsky model in this test case.

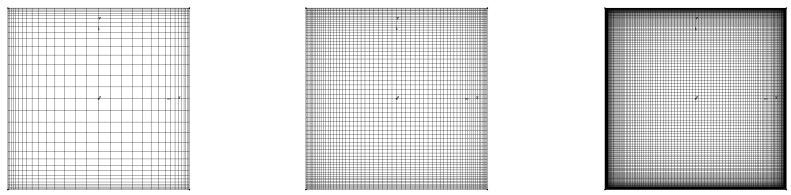

(a) (b) (c)

Figure 21: A series of refined grids, $32 \times 32 \times 16$, $64 \times 64 \times 32$, and $128 \times 128 \times 64$, for large-eddy simulation of a flow in lid-driven cavity at $Re = 10,000$, $x - y$ plane.

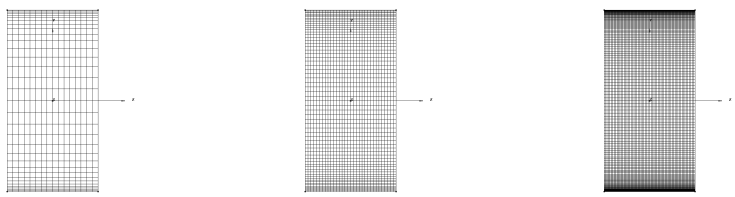

(a) (b) (c)

Figure 22: A series of refined grids, $32 \times 32 \times 16$, $64 \times 64 \times 32$, and $128 \times 128 \times 64$, for large-eddy simulation of a flow in lid-driven cavity at $Re = 10,000$, $z - y$ plane.

4. Conclusion

A set of RANS and LES turbulence models implemented in the flow solver suite Hydra-TH have been used to compute a series of classical, well-documented incompressible flow problems. Computational results obtained in these test cases indicate that the turbulence models in Hydra-TH is able to offer a reliable numerical prediction which agrees well with either the available analytical solution or experimental data. Future efforts will be focused on the verification and validation of more complex flow environment and multi-phase flow problems.

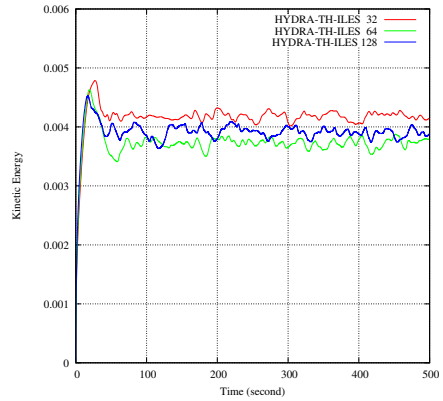

Figure 23: Time history of global kinetic energy for large-eddy simulation of a flow in lid-driven cavity at $Re = 10,000$, obtained on a series of refined grids, $32 \times 32 \times 16$, $64 \times 64 \times 32$, and $128 \times 128 \times 64$, using ILES model.

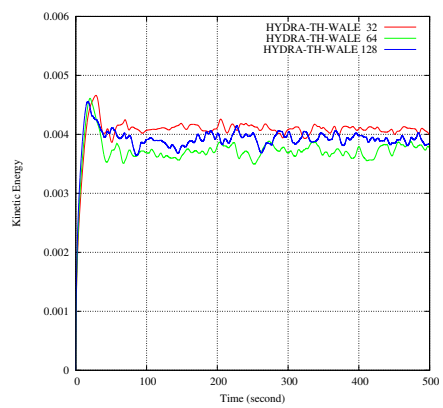

Figure 24: Time history of global kinetic energy for large-eddy simulation of a flow in lid-driven cavity at $Re = 10,000$, obtained on a series of refined grids, $32 \times 32 \times 16$, $64 \times 64 \times 32$, and $128 \times 128 \times 64$, using WALE model.

Acknowledgement

This research was supported by the Consortium for Advanced Simulation of Light Water Reactors (http://www.casl.gov), an Energy Innovation Hub (http://www.energy.gov/hubs) for Modeling and Simulation of Nuclear Reactors under U.S. Department of Energy Contract No. DE-AC05-00OR22725.

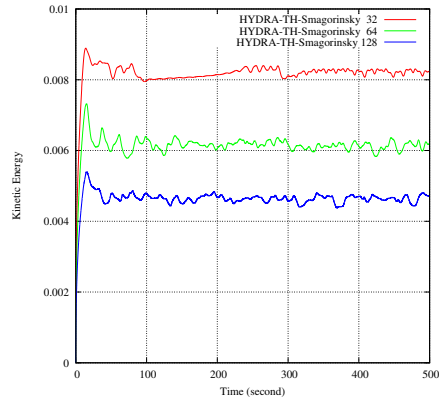

Figure 25: Time history of global kinetic energy for large-eddy simulation of a flow in lid-driven cavity at $Re = 10,000$, obtained on a series of refined grids, $32 \times 32 \times 16$, $64 \times 64 \times 32$, and $128 \times 128 \times 64$, using Smagorinsky model.

References

[1] Christon MA. Hydra-TH Theory Manual. Tech. Rep.; Los Alamos National Laboratories, Los Alamos, New Mexico, LA-UR-11-05387; 2011.

[2] Christon MA, Bakosi J, Lowrie RB. Hydra-TH User's Manual, Version: LA-CC-11120, Dated: December 1, 2011. Tech. Rep.; Los Alamos National Laboratory (LANL); 2012.

[3] Christon MA, Baksoi J, Barnett N, Francois MM, Lowrie RB, Sankaran R. Integration of Hydra-TH in VERA (L2 Milestone THM. CFD. P5. 01). Tech. Rep.; Los Alamos National Laboratory (LANL); 2012.

[4] Bakosi J, Christon MA, Francois MM, Lowrie RB, Nourgaliev R. GTRF Calculations Using Hydra-TH (L3 Milestone THM. CFD. P5. 05). Tech. Rep.; Los Alamos National Laboratory (LANL); 2012.

[5] Bakosi J, Christon MA, Pritchett-Sheats L, Nourgaliev R. Hydra-TH Advanced Capabilities (L3 Milestone THM. CFD. P6. 01). Tech. Rep.; Los Alamos National Laboratory (LANL); 2013.

[6] Bakosi J, Christon MA, Pritchett-Sheats L, Nourgaliev R. Meshing, GTRF, Hydra-TH Performance. Tech. Rep.; Los Alamos National Laboratory (LANL); 2013.

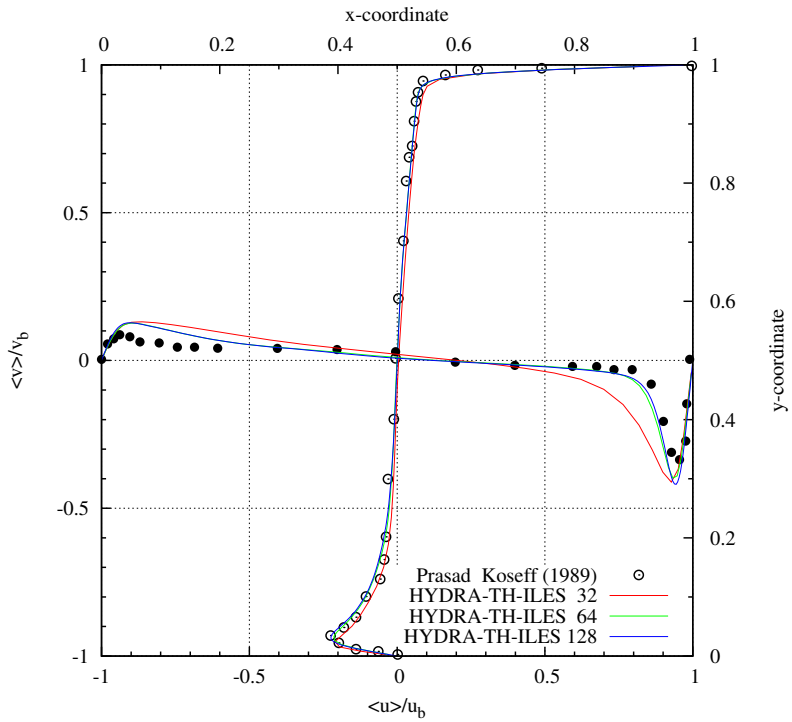

Figure 26: Comparisons of mean velocity components $\langle u \rangle / u_b$ and $\langle v \rangle / u_b$ in the spanwise mid-plane with experimental data for large-eddy simulation of a flow in lid-driven cavity at $Re = 10,000$, obtained on a series of refined grids, $32 \times 32 \times 16$, $64 \times 64 \times 32$, and $128 \times 128 \times 64$, using ILES model.

[7] Bakosi J, Christon MA, Francois MM, Lowrie RB, Nourgaliev R. THM-GTRF: New Spider meshes, New Hydra-TH runs. Tech. Rep.; Los Alamos National Laboratory (LANL); 2012.

[8] Christon MA, Bakosi J, Francois MM, Lowrie RB, Nourgaliev R. Multiphase Flow Analysis in Hydra-TH. Tech. Rep.; Los Alamos National Laboratory (LANL); 2012.

[9] Christon MA. Thermal Hydraulics Methods and Hydra-TH Development. Tech. Rep.; Los Alamos National Laboratory (LANL); 2013.

[10] CASL: the Consortium for Advanced Simulation of Light Water Reactors. 2013. URL `http://www.casl.gov/`.

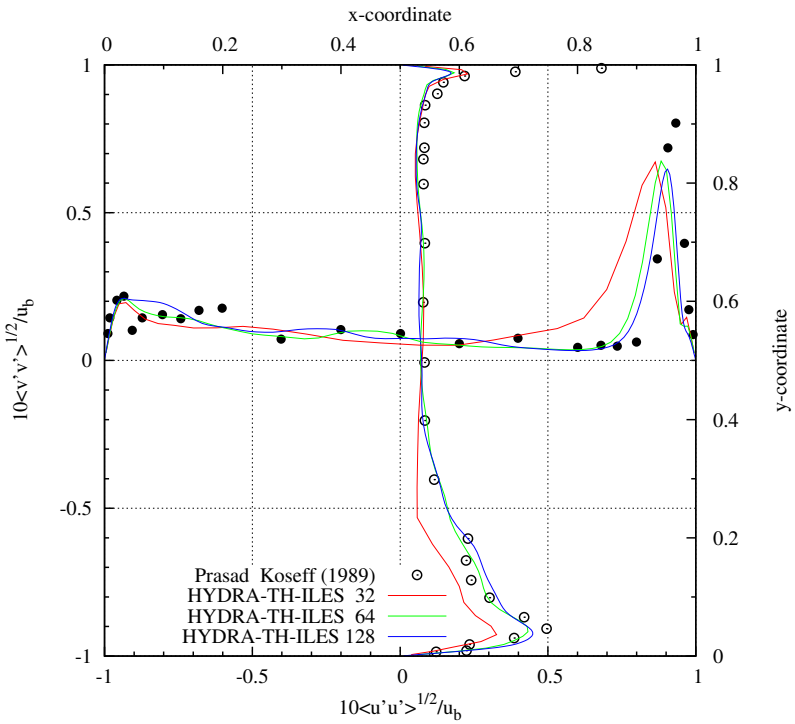

Figure 27: Comparisons of scaled RMS velocity components $10\sqrt{\langle u'u' \rangle}/u_b$ and $10\sqrt{\langle v'v' \rangle}/u_b$ in the spanwise mid-plane with experimental data for large-eddy simulation of a flow in lid-driven cavity at $Re = 10,000$, obtained on a series of refined grids, $32 \times 32 \times 16$, $64 \times 64 \times 32$, and $128 \times 128 \times 64$, using ILES model.

[11] Balay S, Brown J, Buschelman K, Eijkhout V, Gropp W, Kaushik D, et al. PETSc Users Manual Revision 3.3 2012;.

[12] Heroux MA, Bartlett RA, Howle VE, Hoekstra RJ, Hu JJ, Kolda TG, et al. An overview of the Trilinos project. ACM Transactions on Mathematical Software (TOMS) 2005;31(3):397–423.

[13] Spalart P, Allmaras S. A one equation turbulence model for aerodinamic flows. AIAA Journal 1992;94.

[14] Orszag SA, Yakhot V, Flannery WS, Boysan F, Choudhury D, Maruzewski J, et al. Renormalization group modeling and turbulence simulations. Near-wall turbulent flows 1993;:1031–46.

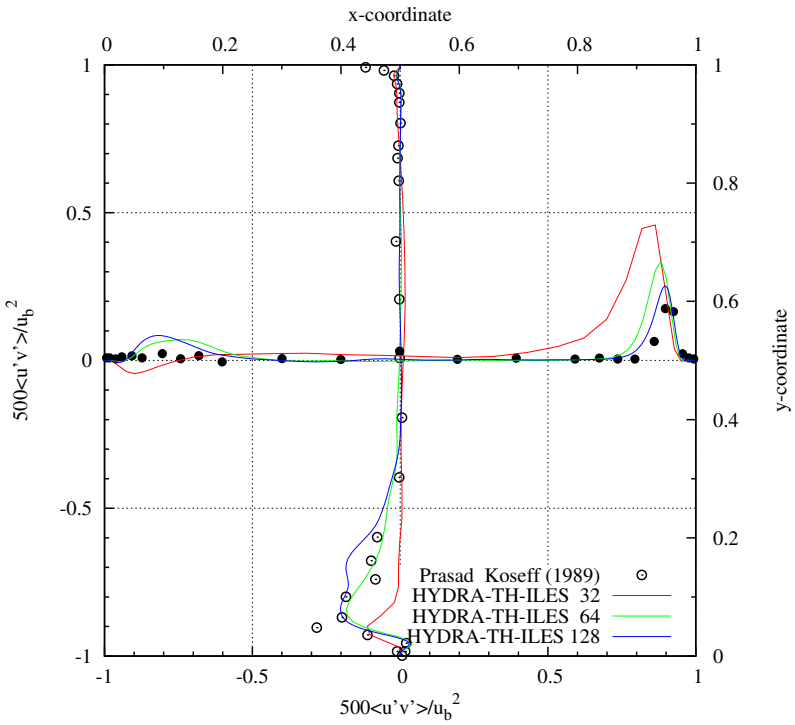

Figure 28: Comparisons of scaled Reynolds stress tensor components $500\langle u'v'\rangle/u_b^2$ in the spanwise mid-plane with experimental data for large-eddy simulation of a flow in lid-driven cavity at $Re = 10,000$, obtained on a series of refined grids, $32 \times 32 \times 16$, $64 \times 64 \times 32$, and $128 \times 128 \times 64$, using ILES model.

[15] Grinstein FF, Margolin LG, Rider WJ. Implicit large eddy simulation: computing turbulent fluid dynamics. Cambridge University Press; 2007.

[16] Smagorinsky J. General circulation experiments with the primitive equations. Monthly weather review 1963;91(3):99–164.

[17] Nicoud F, Ducros F. Subgrid-scale stress modelling based on the square of the velocity gradient tensor. Flow, Turbulence and Combustion 1999;62(3):183–200.

[18] Moser RD, Kim J, Mansour NN. Direct numerical simulation of turbulent channel flow up to $\mathrm{Re}_\tau = 590$. Physics of fluids 1999;11(4):943–5.

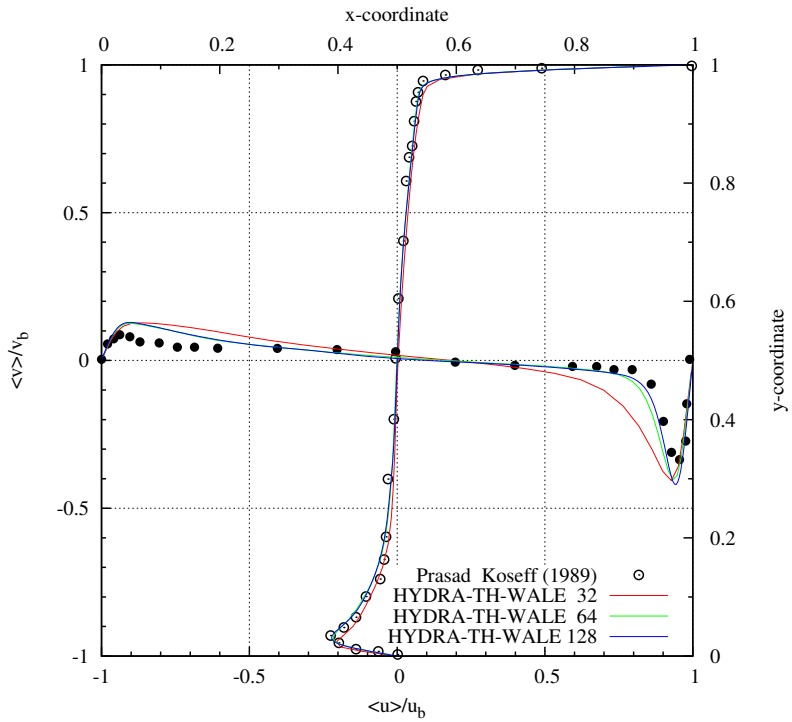

Figure 29: Comparisons of mean velocity components $\langle u \rangle / u_b$ and $\langle v \rangle / u_b$ in the spanwise mid-plane with experimental data for large-eddy simulation of a flow in lid-driven cavity at $Re = 10,000$, obtained on a series of refined grids, $32 \times 32 \times 16$, $64 \times 64 \times 32$, and $128 \times 128 \times 64$, using WALE model.

[19] Prasad AK, Koseff JR. Reynolds number and end-wall effects on a lid-driven cavity flow. Physics of Fluids A: Fluid Dynamics 1989;1(2):208 –19.

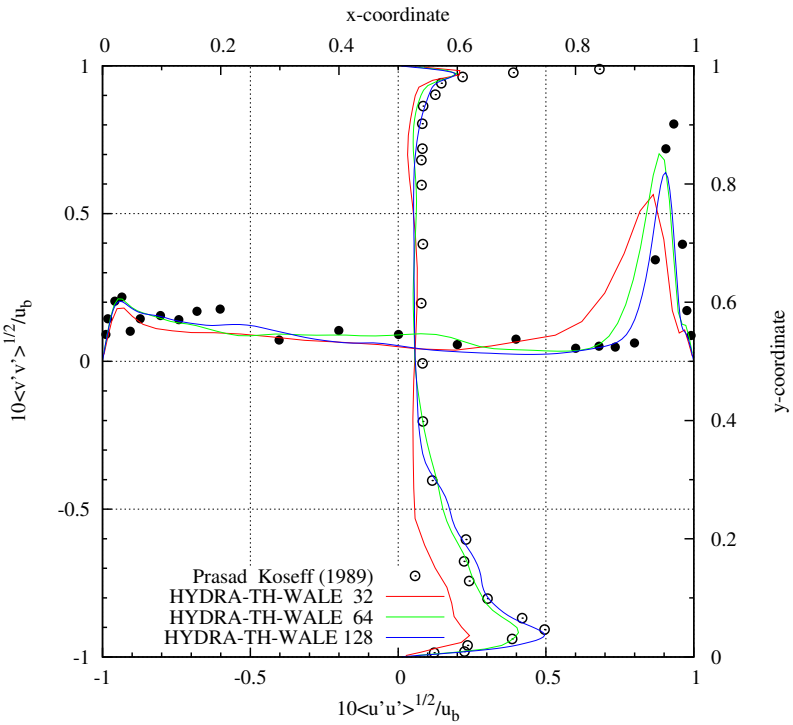

Figure 30: Comparisons of scaled RMS velocity components $10\sqrt{\langle u'u' \rangle}/u_b$ and $10\sqrt{\langle v'v' \rangle}/u_b$ in the spanwise mid-plane with experimental data for large-eddy simulation of a flow in lid-driven cavity at $Re = 10,000$, obtained on a series of refined grids, $32 \times 32 \times 16$, $64 \times 64 \times 32$, and $128 \times 128 \times 64$, using WALE model.

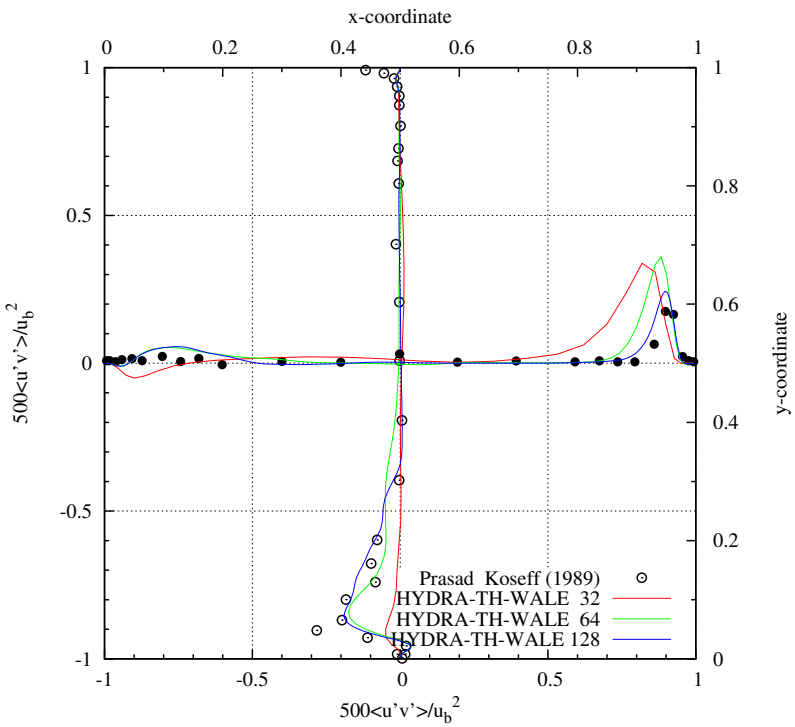

Figure 31: Comparisons of scaled Reynolds stress tensor components $500\langle u'v'\rangle/u_b^2$ in the spanwise mid-plane with experimental data for large-eddy simulation of a flow in lid-driven cavity at $Re = 10,000$, obtained on a series of refined grids, $32 \times 32 \times 16$, $64 \times 64 \times 32$, and $128 \times 128 \times 64$, using WALE model.

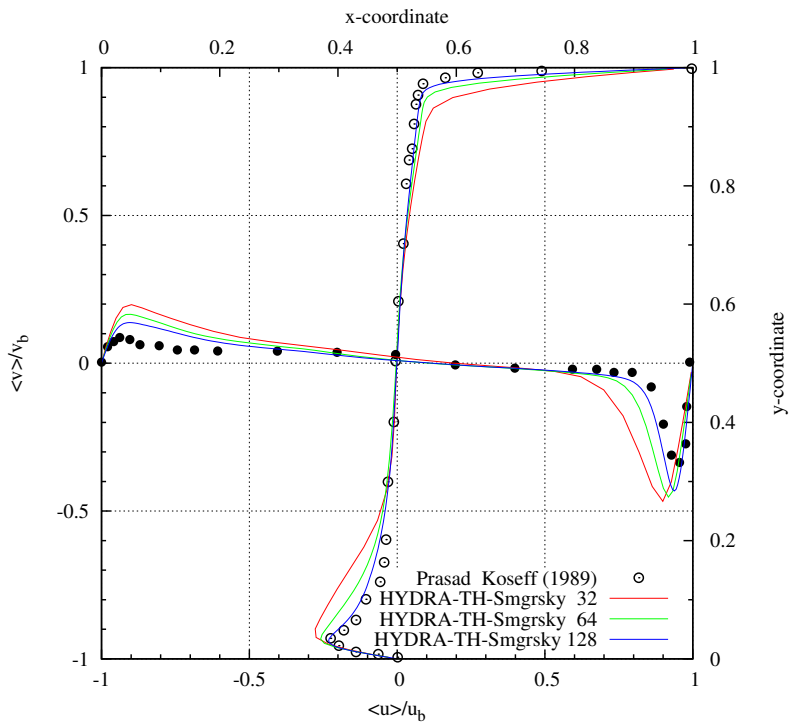

Figure 32: Comparisons of mean velocity components $\langle u \rangle / u_b$ and $\langle v \rangle / u_b$ in the spanwise mid-plane with experimental data for large-eddy simulation of a flow in lid-driven cavity at $Re = 10,000$, obtained on a series of refined grids, $32 \times 32 \times 16$, $64 \times 64 \times 32$, and $128 \times 128 \times 64$, using Smagorinsky model.

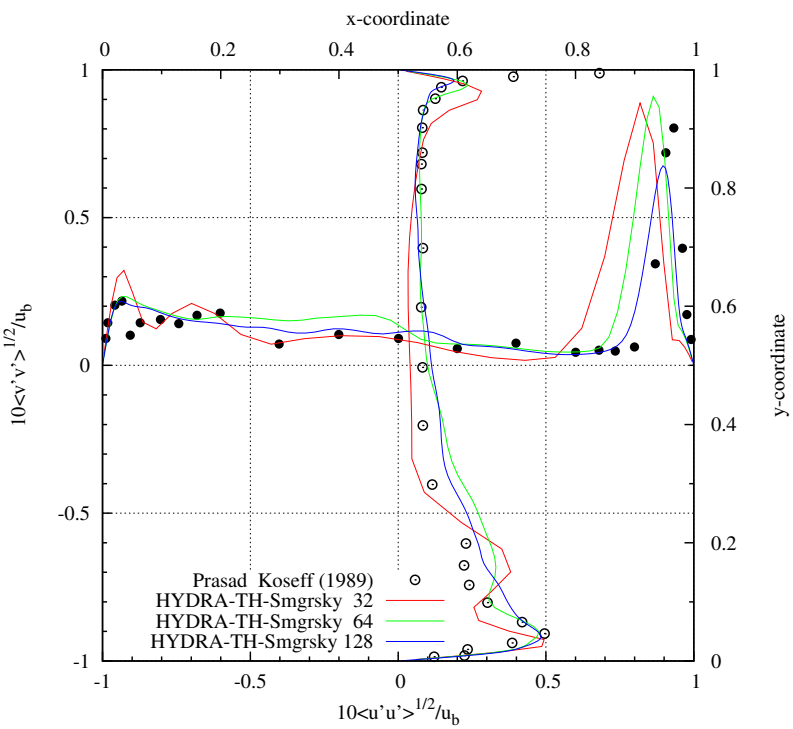

Figure 33: Comparisons of scaled RMS velocity components $10\sqrt{\langle u'u' \rangle}/u_b$ and $10\sqrt{\langle v'v' \rangle}/u_b$ in the spanwise mid-plane with experimental data for large-eddy simulation of a flow in lid-driven cavity at $Re = 10,000$, obtained on a series of refined grids, $32 \times 32 \times 16$, $64 \times 64 \times 32$, and $128 \times 128 \times 64$, using Smagorinsky model.

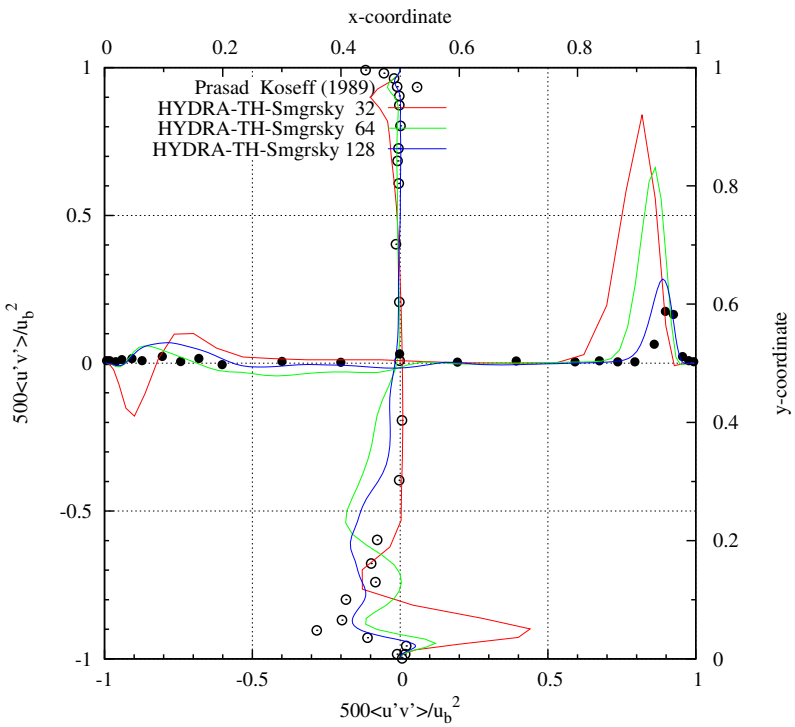

Figure 34: Comparisons of scaled Reynolds stress tensor components $500\langle u'v'\rangle/u_b^2$ in the spanwise mid-plane with experimental data for large-eddy simulation of a flow in lid-driven cavity at $Re = 10,000$, obtained on a series of refined grids, $32 \times 32 \times 16$, $64 \times 64 \times 32$, and $128 \times 128 \times 64$, using Smagorinsky model.